Detailed numerical simulation of landslide dam failure considering non-uniform and multi-layered sediments: A case study of the second Baige landslide dam in the Jinsha River, China

Abstract

Prediction of the dam failure process and downstream flooding is crucial for hazard management and understanding the local morphological changes associated with landslide dam events. Indeed, numerous models exist to simulate landslide dam failures, but the characteristics of these dams, especially their very specific material composition, are often oversimplified or neglected. This paper presents a 2D numerical model that accounts for non-uniform and multi-layered sediments. It is applied to the failure of the second Baige landslide dam and the results are validated through comparisons with field observations. The effects of the upstream inflow rate and dam material composition on the failure process are investigated. Additionally, the numerical results are compared to those obtained from five other detailed, less detailed or empirical models. The results show that the proposed model accurately reproduces the dam failure process and captures the evolution of surface grain size distribution during the event. Increased upstream inflow rates significantly increase the peak discharge but have a limited effect on the final breach while lower inflow rates significantly extend the time to failure, allowing for emergency interventions and evacuation. Due to the high inflow discharge in the case of the Baige event and relatively fine dam material, all sediment sizes are mobilized, resulting in negligible differences in failure evolution between uniform and non-uniform sediment scenarios. Furthermore, unlike empirical and simplified numerical models, the proposed model does not rely on limited case studies or predefined breach evolution assumptions, providing a more reliable simulation framework. It therefore offers a practical and flexible framework for hazard assessment and mitigation planning in mountainous regions worldwide.

Keywords

Baige landslide dam, Numerical simulation, Shallow water equation, Material composition, Dam failure process, non-uniform and multi-layered sediments

1. Introduction

Landslide dams are common natural hazards in mountainous areas and are formed by the blockage of rivers with landslides, rockfalls and debris flows (Costa and Schuster 1988). Over the past two decades, intense tectonic activity and extreme weather have contributed to numerous landslide dam events in mountainous countries such as Japan, Nepal, and China (Zheng et al. 2021). For example, the 2004 Mid-Niigata Prefecture earthquake in Japan triggered 45 landslide dams (Sassa 2005). while the 2008 Wenchuan earthquake in China generated over 200 landslide dams (Yin et al. 2009). More recent examples include the Jure landslide dam caused by heavy rainfall in Nepal in 2014 (Van Tien et al. 2021) and the two Baige landslide dams formed by prolonged precipitation on the Tibet–Sichuan border in 2018 (Ouyang et al. 2019). Unlike artificial dams, most landslide dams fail within a month after their formation, resulting in catastrophic downstream flooding and significant environmental change (Korup 2004). For example, the failure of the Tangjiashan landslide in China in 2008 deposited several meters of sediment and altered the downstream river channel (Yin et al. 2009). The Baige landslide dams endangered over 20,000 people and caused economic loss estimated at 42 billion CNY in the downstream areas (Yang et al. 2022). Previous studies have shown that the downstream impact of landslide dam failure is largely determined by factors such as peak discharge and the failure mechanism (Delaney and Evans 2015). Accurate prediction of these factors is therefore essential for effective hazard management.

Landslide dam failure prediction is typically conducted using empirical equations, physically based simplified models, and, in some cases, detailed numerical simulations (Mei et al. 2022). Empirical equations—such as those developed by Walder and O'Connor (1997) and Shen et al. (2020)—primarily aim to estimate key failure parameters like the peak discharge. These equations are derived from statistical analyses of historical landslide dam events. However, their reliability is often questioned due to their reliance on a limited set of geometric parameters and a relatively small dataset, which may not capture the full complexity of real-world scenarios (Froehlich 2022). Physically based simplified models were initially designed for artificial dam failures, such as the BREACH model, which employs the broad-crested weir assumption for discharge calculation and uses an empirical breach pattern to simulate the failure process (ASCE/EWRI Task Committee on Dam/Levee Breaching, 2011). Building on these foundational models, more recent efforts have adapted them for landslide dams. For example, the DABA model proposed by Chang and Zhang (2010) and the DB-IWHR model proposed by Zhong et al. (2019) have been used in various case studies and have demonstrated reasonable accuracy in predicting the failure process (Shi et al. 2016; Wang et al. 2021). Nevertheless, their predictive capabilities are limited by predefined breach patterns and specific breach depths, limiting their application in predicting the actual failure.

Detailed numerical models that solve various forms of the shallow water equations (e.g., 1D and 2D), often coupled with sediment transport and morphological change algorithms, have been widely applied to simulate river-related processes such as flood propagation, topographic evolution, and sediment dynamics (Soares-Frazão et al. 2012, Qian et al. 2017; Hashemi et al. 2023; Thapa et al. 2024). Numerous models have been developed that incorporate different sediment transport modes and numerical schemes (Simpson and Castelltort 2006; Wu and Wang 2007; Soares-Frazão & Zech 2010; García-Navarro et al. 2019; Zhao et al. 2019). For example, models that couple the shallow water equations with an active layer formulation can effectively simulate morphological changes involving non-uniform sediments (Stecca et al. 2014; Juez et al. 2015; Chavarrías et al. 2019; Yang et al. 2024b). Some models also incorporate the Richards equation to account for both surface and subsurface flows during dike failure or flood propagation (Li et al. 2021; Delpierre et al. 2023). In addition, multiphase models, such as two-phase or quasi-single-phase formulations, that treat solid and fluid components separately have been developed for sediment-laden flows (Pudasaini 2012; Xia et al. 2018; Martínez-Aranda et al. 2022; Meurice and Soares-Frazão 2024). Despite their proven accuracy in a range of riverine and geomorphic contexts, these models have only been rarely applied to simulate landslide dam failures and the resulting downstream flood and morphological changes. In particular, most of these models do not explicitly consider the unique characteristics of landslide dams, which can lead to significant inaccuracies in simulation outcomes. Indeed, the landslide material is deposited without compaction in the valley to form the dam, which leads to a wide material composition and a low safety factor for the resulting embankment. Recently, three-dimensional (3D) models based on the Naiver–Stokes equations have also been employed to simulate landslide dam failures, such as open-source 3D models applied by Mei et al. (2021) or Hu et al. (2024) to both laboratory-scale and real-world scenarios. In addition, Smoothed Particle Hydrodynamics (SPH)-based models have been validated using small-scale dam failure experiments (Zhou et al, 2024). However, the computational cost of such models remains prohibitively high for large-scale applications. As a result, 2D shallow-water based numerical models remain the most practical and efficient option for large-scale simulations of landslide dam failures and the associated downstream impacts. Nevertheless, further validation is needed to assess their accuracy and reliability in capturing the complex processes involved in such events.

In this paper, a detailed 2D numerical model based on the shallow-water and Exner equations, considering non-uniform and multi-layered sediments, is applied to simulate a landslide dam failure. Additionally, the effects of the upstream inflow rate and dam material composition on the dam failure process are analyzed through simulations of the second Baige landslide dam event. The paper is organized as follows: Section 2 introduces the second Baige landslide dam and the available data, including the digital elevation model of the study area and the composition and distribution of dam materials. Section 3 describes the numerical model used to simulate the Baige dam failure, along with the numerical setup and the simulation scenarios. Section 4 presents the simulation results, the evaluation of the model's performance, and discusses the impact of the upstream inflow rate and of the dam material composition on the failure process. In Section 5, results from the proposed model are compared with those from empirical equations, simplified physically based models, and other detailed numerical approaches. The limitations of the current model and directions for future development are also discussed. Finally, Section 6 summarizes the main conclusions of the study.

2. Description of the study area

2.1. The two co-site Baige landslide dams

As illustrated in Figure 1, the Jinsha River is the upper reach of the Yangtze River, located in southwestern China. It originates in Qinghai province and flows through Tibet, Sichuan and Yunnan Provinces, spanning a total length of approximately 2,290 km (Figure 1b) (Tan et al, 2024). Due to the uplift of the Tibetan Plateau and the deep incision caused by river erosion, the river channel is steep and characterized by highly energetic flows. These geomorphological and hydrological conditions have led to frequent natural hazards in the region, including landslides, rockfalls, and debris flows. According to a statistical study by Li et al, (2016), more than 339 landslides and rockfalls have been documented along the Jinsha River, with 61 of these events resulting in river blockage and the formation of landslide dams. Furthermore, the significant elevation difference of approximately 3,250 meters creates favorable conditions for hydropower development. As a result, over 25 large artificial dams have been constructed or planned along the river for energy production and flood control (Zhang et al, 2019). Given these conditions, the analysis of landslide dam-induced floods and the implementation of effective hazard management strategies are critical for the safety of local populations and infrastructure.

The two Baige landslide dams were formed on the upper reaches of the Jinsha River (98°42'17" E, 31°04'59" N), approximately 20 km downstream of the Boluo village, on 10 October and 4 November 2018, respectively (Figure 1b). The first dam failed two days after its formation and had no impact on the downstream areas (Figure 1c). Following its failure, a residual dam approximately 29 meters high remained in place. The second Baige landslide, with a volume of 1.20×10^{7} m^3, was deposited directly on the remnants of the first dam, creating a second, larger landslide dam. This second dam was 96 m high with a 79.4 m wide crest, and had a total volume of 3.02×10^{7} m^3 (Figure 1c), impounding an upstream lake with a maximum capacity of 7.50×10^{8} m^3. Due to the increased risk posed by the larger lake volume, the upstream inflow rate, controlled by dams in the upper valley, was reduced from 1,600 m^3/s to 800 m^3/s to delay the failure of the landslide dam. In addition, a diversion channel with a depth of 15 m, a top width of 42 m and a bottom width of 3 m was excavated along the dam crest (Figure 1d), successfully reducing the lake capacity to 5.24×10^{8} m^3 (Yang et al. 2022). Despite these mitigation efforts, the second Baige landslide dam failed 9 days after its formation, with a peak discharge of 33,900 m^3/s. The resulting flood traveled over 600 km downstream. Post-failure observations indicated the presence of a residual dam with a height of 35 m. The final breach was estimated to be 61 m deep, with a top width of 300 m and a bottom width of 90 m (Zhang et al. 2019).

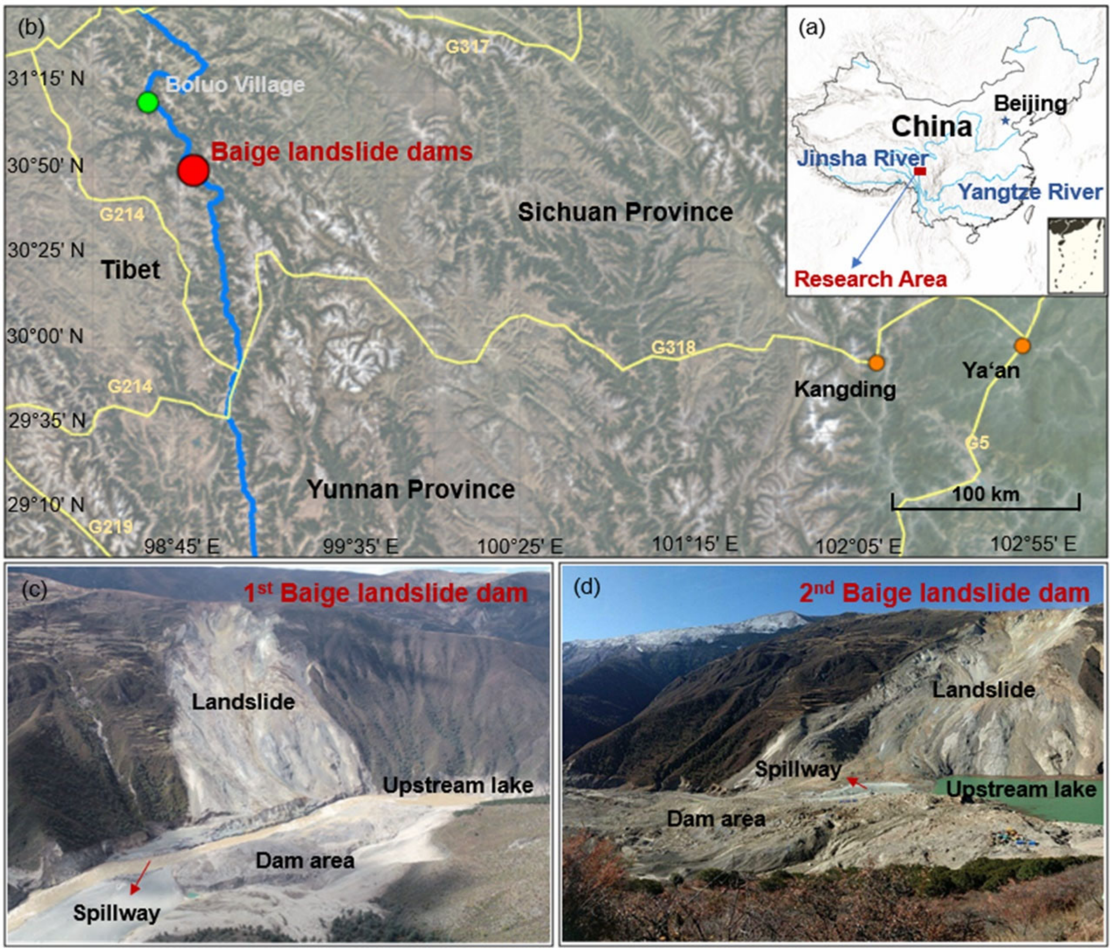

Figure 1 The two Baige landslide dams on the Jinsha River, China: (a) Location of the Jinsha River; (b) Location of the two Baige landslide dams; (c) The first Baige landslide dam formed on 10 October, 2018 and (d) The second Baige landslide dam formed on 4 November, 2018.

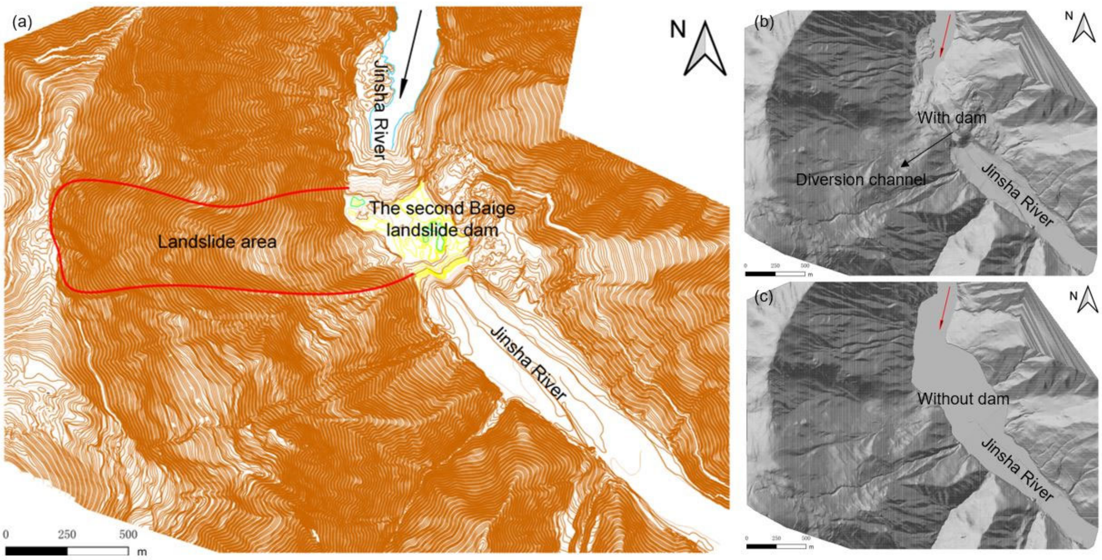

Figure 2 Regional digital elevation model of the second Baige landslide dam: (a) Topographic contour map of the second Baige landslide dam; (b) DEM before dam failure and (c) DEM after dam failure.

2.2. Digital terrain model of the second Baige landslide dam

The regional digital elevation model (DEM) used in this study, representing the topography after the formation of the second Baige landslide dam, is shown in Figure 2a. As the simulation focuses specifically on the failure of the second Baige landslide dam, a DEM covering an area of 2.9×2.2 km^2 was used to conduct the simulation. Within this domain, the Jinsha River extends for approximately 2.8 km, with the landslide dam situated near the center of the simulation area. To incorporate the effects of emergency mitigation measures, a diversion channel with a depth of 15 m, a top width of 42 m and a bottom width of 3 m was added to the DEM (Figure 2b), replicating the channel excavated during the actual event. As no DEM was available for the region prior to the formation of the landslide dams, the post-event DEM was manually modified based on available topographic and geological data to reconstruct the pre-dam topography corresponding to the second landslide dam (Figure 2c). The DEM containing the dam and the diversion channel (Figure 2b) was used to define the erodible morphology of the landslide dam while the modified DEM representing the pre-event terrain (Figure 2c) was used to represent the non-erodible bed in the numerical simulation.

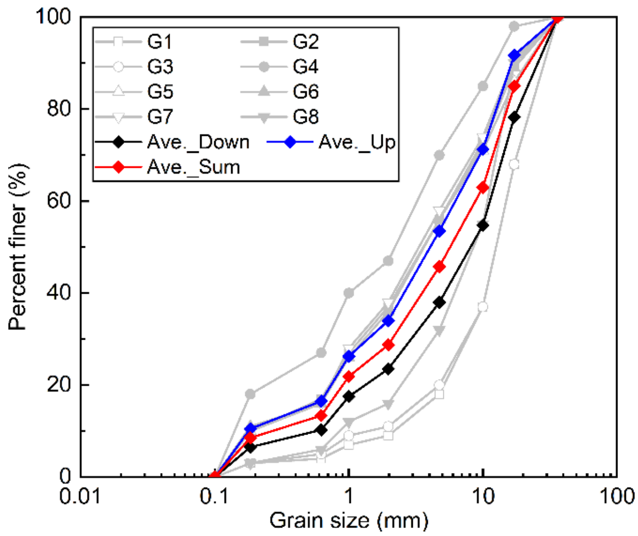

Figure 3 Dam material composition of the second Baige landslide dam. Note: G1, G3, G5 and G7 are samples from the elevation below 2940 m; G2, G4, G6 and G8 are samples from the elevation above 2940 m. Ave._Up and Ave._Down refers to the average value of the materials from the elevation above and below 2940 m, respectively. Ave._Sum is the average of the all eight samples.

2.3. Dam material composition and distribution

Dam material composition is one of the factors influencing the failure of landslide dams (Shen et al., 2022). Based on a field survey by Zhang et al. (2019), eight samples were collected from various locations within the second Baige landslide dam for analysis (Figure 3). The upper portion of the dam, located between elevations of 2,940 m and 2,970 m, consisted of loose gravelly sand, with a dry density ranging from 1469 – 1591 kg/m^3 and a void ratio between 0.41 and 0.46 (Samples G1, G3, G5 and G7 shown in Figure 3). The lower section of the dam, situated below 2,940 m, was predominantly composed of weathered plagioclase gneiss, exhibiting a higher dry density of 1831 – 2062 kg/m^3 and a porosity ranging from 0.24 to 0.32 (Samples G2, G4, G6 and G8 shown in Figure 3). The particle size of the dam material varied from 0.075 mm to 40 mm. The median diameter was 4.3 mm for the upper layer and 8.6 mm for the lower layer, with an estimated average of 6.2 mm for the entire dam. The angle of repose for the dam material was estimated to range from 35° to 38°, as estimated by Li et al, (2023) and Mei et al, (2022).

3. Methodology

3.1. Numerical model considering non-uniform and multi-layered sediments

The failure of the second Baige landslide dam was simulated using a two-dimensional numerical model that accounts for non-uniform and multi-layered sediment dynamics. A schematic of the model framework is presented in Figure 4. This model integrates the shallow water equations with a modified Exner equation and Hirano's active layer formulation to capture sediment transport and morphological evolution processes (Figures 4a and 4b). The governing equations used in the numerical model are as follows:

$$\frac{\partial h}{\partial t} + \frac{\partial (q_x)}{\partial x} + \frac{\partial (q_y)}{\partial y} = 0 \tag{1}$$

$$\frac{\partial(q_x)}{\partial t}+\frac{\partial(q_x^2/h+\frac{1}{2}gh^2)}{\partial x}+\frac{\partial(q_xq_y/h)}{\partial y}=gh\left(-\frac{\partial z_b}{\partial x}-\frac{n^2\sqrt{u^2+v^2}u}{h^{4/3}}\right) \quad (2)$$

$$\frac{\partial(q_y)}{\partial t}+\frac{\partial(q_xq_y/h)}{\partial x}+\frac{\partial(q_y^2/h+\frac{1}{2}gh^2)}{\partial y}=gh\left(-\frac{\partial z_b}{\partial y}-\frac{n^2\sqrt{u^2+v^2}v}{h^{4/3}}\right) \quad (3)$$

$$\frac{\partial z_b}{\partial t}+\frac{1}{1-\varepsilon}\frac{\partial(\sum_{i=1}^{N}f_iq_{si,x})}{\partial x}+\frac{1}{1-\varepsilon}\frac{\partial(\sum_{i=1}^{N}f_iq_{si,y})}{\partial y}=0 \quad (4)$$

$$\frac{\partial(f_iL_a)}{\partial t}=-\frac{1}{1-\varepsilon}\left(\frac{\partial(f_iq_{si,x})}{\partial x}+\frac{\partial(f_iq_{si,y})}{\partial y}\right)-f_{esi}\frac{\partial(z_b-L_a)}{\partial t} \quad (5)$$

where Eqs. (1), (2) and (3) are the mass conservation and momentum equations and are used to update the flow field during the simulation, with h, z_b, n, g, $q_x=uh$, $q_y=vh$ being the flow depth, bed level, Manning friction coefficient, gravitational acceleration, unit discharge in x and y directions, respectively, with u and v the x and y velocity components. Eq. (4) is the modified Exner equation considering non-uniform sediments, where ε, N, f_i, $q_{si,x}$ and $q_{si,y}$ are the bed porosity, the number of considered sediment fractions, the percentage content of the i^{th} sediment fraction, the unit sediment transport rates of the i^{th} sediment fraction in the x and y directions, respectively. Eq. (5) is the active layer equation and is used to update the percentage content of each sediment fraction in the active layer, with L_a being the active layer depth, f_{esi} being the sediment exchange between the bed load layer and the active layer (Figure 4) and can be estimated as follow:

$$f_{esi}=\begin{cases}F_i & if\ degradation\\ af_i+(1-a)\dfrac{f_i\sqrt{q_{si,x}^2+q_{si,y}^2}}{q_s} & if\ aggradation\end{cases} \quad (6)$$

where a is an empirical parameter ranging from 0 to 1 and q_s is the total bedload sediment transport rate.

The model is solved with a set of closure equations to calculate the sediment transport rate, the active layer depth, and the updated Manning coefficient that evolves according to the changing bed material composition. In addition, a bank failure module proposed by Swartenbroekx et al. (2010)

is applied during the simulation (Figure 4c). This bank failure module allows to simulate the lateral slope collapse of the breach during the landslide dam failure, thereby improving the accuracy of both the failure process prediction and the peak discharge estimation (Evangelista et al, 2015). A weakly coupled finite volume scheme (Franzini and Soares-Frazão 2016) was used to solve the governing equations. The model's applicability and accuracy were tested by simulating both a dam-break flow and a dam failure at the experimental scale, as detailed in Yang et al. (2024b).

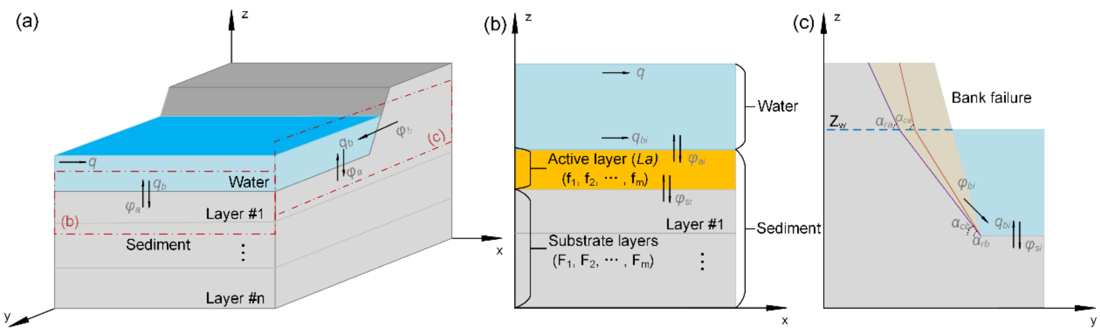

Figure 4 Sketch of the numerical model considering non-uniform and multi-layered sediments: (a) overview of the model; (b) the active layer module and (c) the bank failure module. Note: q is the discharge, q_b and q_{bi} are the bedload transport rate for the total sediment and for each fraction of the sediment. φ_a and φ_b are the interactions of bedload with sediment bed and bank material, respectively. φ_{ai} and φ_{bi} are the interaction of bedload with each fraction of the sediment bed and bank material. φ_{ai} is the interaction between the active layer and substrate layer in each fraction of the sediment. α_{ca} and α_{cb} are the critical angles above and below the water level. α_{ra} and α_{rb} are the residual angles above and below the water level Z_w.

3.2. Numerical set-up

The computational domain used for simulating the failure of the second Baige landslide dam is shown in Figure 5. The formation of the second Baige landslide dam resulted in a large backwater area upstream of the dam (Figure 5a). However, including such a vast backwater area in the numerical simulation would lead to higher computational costs and require a larger regional DEM dataset, which was not feasible. Therefore, only a limited portion of the upstream reservoir area, as indicated in Figure 5b, was included in the computational mesh. To account for the backwater effects in the upstream region, the relationship between the upstream water depth and reservoir volume

(Figure 5d) was used in the simulation. The computational domain was discretized using a series of triangular cells and divided into three distinct sections, as shown in Figure 5c. The first section, representing the main river channel, was discretized with a mesh size of 10 meters. The second section, corresponding to the upstream reservoir and hillslope area, was discretized with a coarser mesh size of 100 meters. The third section, representing the diversion channel at the crest of the dam, had a finer mesh size of 5 meters.

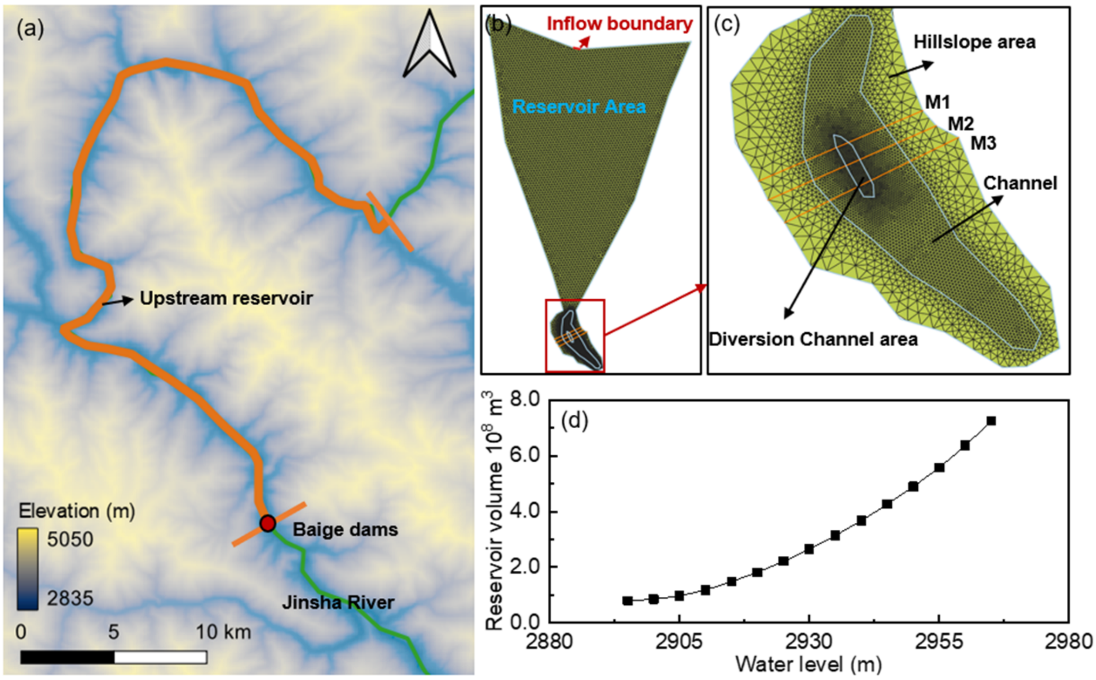

Figure 5 Set-up of the computational domain: (a) The Baige dams and the upstream reservoir; (b) Computational domain and its set-up; (c) Details of the river channel, diversion channel and monitor sections and (d) The relationship between upstream water level and reservoir volume.

A total of 18,800 triangular cells were generated within the computational domain. The initial bed elevations for the non-erodible surface and the erodible dam were assigned to each cell based on the regional DEMs representing the terrain before and after the formation of the landslide dam (Figures 2b and 2c). A 200-meter-long section at the upstream end of the reservoir was designated as the inflow boundary of the computational domain. Additionally, three monitoring sections, M1, M2, and M3, located around the dam crest, were established to record discharge throughout the simulation. These sections were also used to analyze the temporal evolution of the breach geometry during the dam failure process.

Table 1 Numerical scenarios and the related parameters

Scenario	Q_{in}	Dam material parameter									
		L	d_{50}	n	ε	F	P		$d_{50,i}$		L_a
S1	400	1	4.3	0.038	0.46	2	0.6	0.4	1.5	13.1	0.7
		2	8.6	0.042	0.32	2	0.6	0.4	3.3	18.8	
S2	800	1	4.3	0.038	0.46	2	0.6	0.4	1.5	13.1	0.7
		2	8.6	0.042	0.32	2	0.6	0.4	3.3	18.8	
S3	1,200	1	4.3	0.038	0.46	2	0.6	0.4	1.5	13.1	0.7
		2	8.6	0.042	0.32	2	0.6	0.4	3.3	18.8	
S4	1,600	1	4.3	0.038	0.46	2	0.6	0.4	1.5	13.1	0.7
		2	8.6	0.042	0.32	2	0.6	0.4	3.3	18.8	
S5	2,000	1	4.3	0.038	0.46	2	0.6	0.4	1.5	13.1	0.7
		2	8.6	0.042	0.32	2	0.6	0.4	3.3	18.8	
S6	800	1	6.2	0.040	0.45	1	1.0		6.2		-

Note: Q_{in} (m^3/s) is the upstream inflow rate; L is the i^{th} layer of sediments; d_{50} (mm) is the median diameter of each layer; n ($m^{1/3}/s$) is the Manning coefficient; ε is the porosity; F is the fraction number in each layer; P is the percentage content of each sediment fraction in each layer; $d_{50,i}$ (mm) is the median diameter of each sediment fraction in each layer; L_a (m) is the active layer depth.

3.3. Numerical scenarios

To evaluate the capability of the proposed model in simulating the landslide dam failure process, six scenarios were designed with varying upstream inflow rates and dam material compositions. Details of these six scenarios are presented in Table 1. Scenarios S1 to S5 focus on different upstream inflow rates, ranging from 400 m^3/s to 2,000 m^3/s. Among these, S2 (800 m^3/s) and S4 (1,600 m^3/s) correspond to measured values observed before and after emergency mitigation efforts, respectively. In scenarios S2 and S6, different dam material compositions were considered. Scenario S2 employs a two-layer sediment structure, with each layer divided into two sediment fractions to represent the non-uniform grain size distribution. In contrast, Scenario S6 assumes uniform sediment composition throughout the dam, modeled as a single layer. For all scenarios, the material density was set to 2,700 kg/m^3. Manning's roughness coefficients were set to 0.04 $m^{1/3}/s$ for the dam and 0.01 $m^{1/3}/s$ for the reservoir area, in accordance with Li et al, (2023). When simulating non-uniform sediments, an active layer depth of 0.7 meters was considered. The bank failure module evaluated slope stability using an empirical angle of 60° as both the critical and residual angle above the water surface, while a repose angle of 35° was applied for the critical and residual angles below the flow, consistently across all scenarios. To reduce the computational time, a higher inflow rate of 5,000 m^3/s was initially applied to rapidly fill the upstream reservoir. This inflow rate was then reduced to the target scenario-specific value before overtopping began. During each simulation, discharge and related outputs were recorded at 200-second intervals.

4. Results

In this section, the numerical results from Scenario S1 are first compared with the measured data to evaluate the model's performance in simulating the failure of the second Baige landslide dam, particularly under conditions involving non-uniform and multi-layered sediments. The dam failure process, discharge variation, breach evolution, and post-failure surface grain size distribution are analyzed. Subsequently, the simulation results from the six scenarios—featuring different upstream inflow rates and dam material compositions—are compared to assess their influence on the dam failure process and associated discharge dynamics.

4.1. Results of S1

4.1.1. Dam failure process

Figure 6 illustrates the variation in upstream water depth and dam geometry throughout the failure process of the second Baige landslide dam, while Figure 7 presents the changes in upstream reservoir water level and mean discharge at monitoring profiles M1, M2, and M3. It is important to note that the onset of overtopping is defined as t = 0 s, as a higher inflow rate was applied during the reservoir infilling stage to reduce the simulation time. Consequently, the infilling phase is excluded from the following analysis.

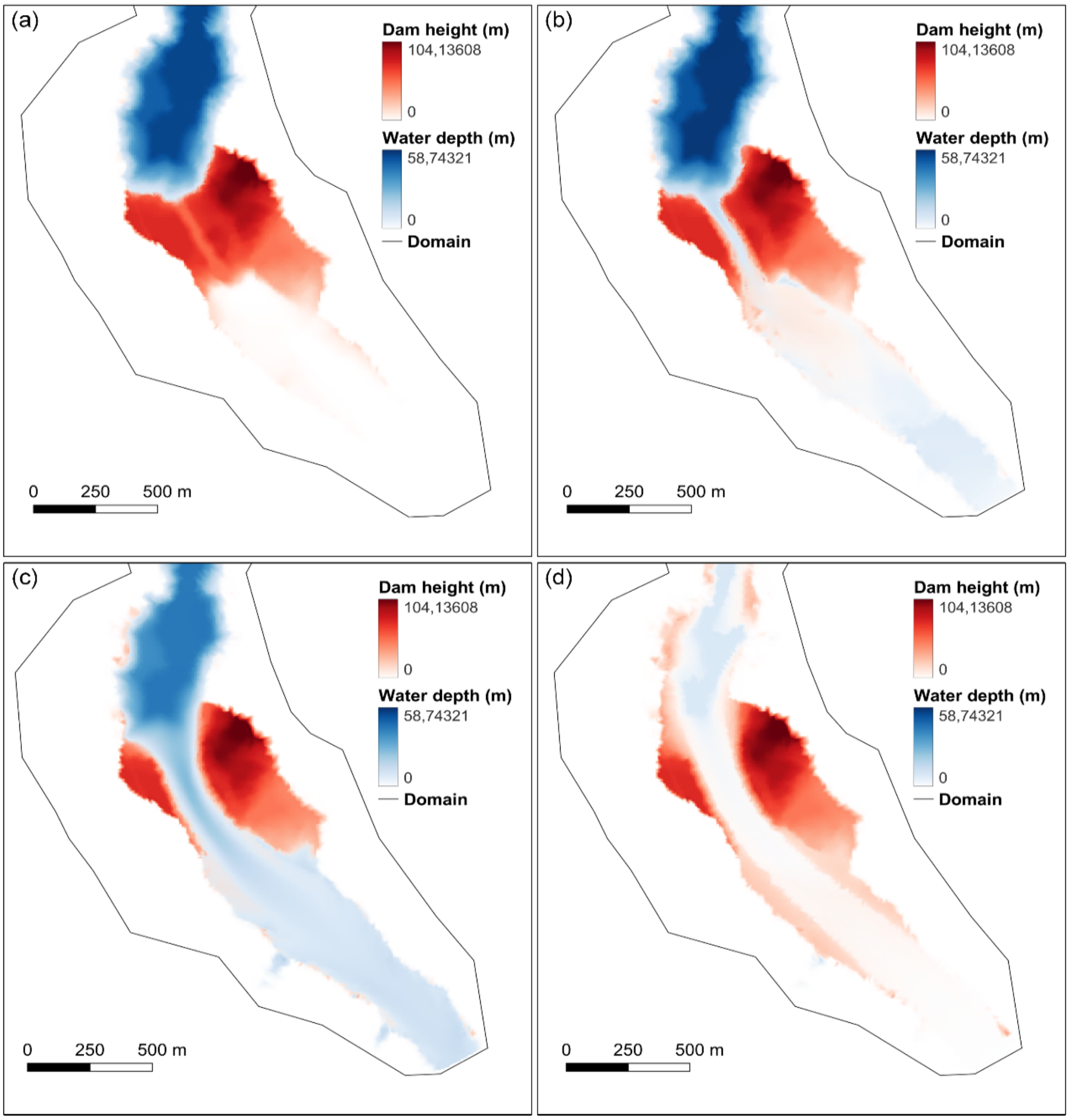

Figure 6 Upstream water level variation and dam failure process: (a) Beginning of overflow in the diversion channel (as t = 0 s); (b) Breach development (t = 82,800 s); (c) Occurrence of peak discharge (t = 100,000 s) and (d) Ending of dam failure simulation (t = 202,600 s).

The overtopping began when the upstream water level reached 2,950.86 m (Figure 7), initiating flow through the diversion channel and triggering dam failure (Figure 6a). The water level continued to rise gradually, peaking at 2,955.73 m at t = 86,400 s. This value closely matches the observed peak of 2,956.40 m, indicating that the simulated reservoir conditions are consistent with field measurements. Concurrently, the breach depth and width expanded progressively (Figure 6b), although the discharge remained relatively low during this initial phase. A rapid increase in discharge was observed after 80,000 s (Figure 7), culminating in a peak discharge of 32,767 m³/s, only 3.4% lower than the measured peak of 33,900 m³/s. The simulated peak occurred at t = 100,000 s, which corresponds to a 2.2-hour deviation from the observed peak time. Following the peak, the discharge declined significantly, while the breach continued to widen and deepen until reaching its final configuration (Figure 6d). At this point, the discharge stabilized to match the upstream inflow rate. The entire failure process concluded at t = 194,400 s, corresponding to a total failure duration of 54 hours. This result aligns well with the reported duration of 51.2 hours (Zhang et al. 2019). A summary comparison between the simulation results and the measured data is provided in Table 2.

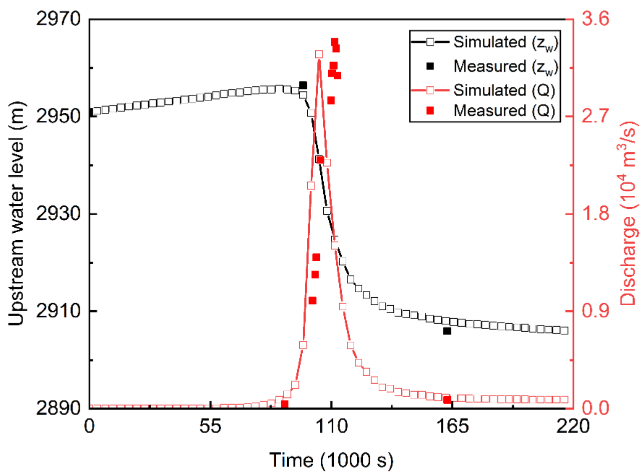

Figure 7 Variation of upstream water level and discharge during dam failure.

3.1.2. Breach evolution and changes in dam topography

The breach evolution plays a critical role in controlling both the dam failure process and the magnitude of downstream flooding (Peng and Zhang, 2012; Takayama et al., 2021). As shown in Figure 8, similar breach development patterns were observed along profiles M1, M2, and M3, which can be divided into three distinct stages. Stage 1 began at the onset of overtopping (t = 0 s) and continued until t = 70,000 s. During this stage, the discharge remained relatively low, resulting in only a slight increase in breach depth, while the breach top width remained nearly constant. Stage

2, from t = 70,000 s to t = 100,000 s, was marked by a rapid increase in discharge. This resulted in significant enlargement of the breach, with both the depth and top width increasing rapidly until reaching their final dimensions. In the third stage (after t = 10,000 s), both the breach depth and top width remained constant. However, the breach bottom width continued to widen gradually until the final breach geometry was reached. The final breach dimensions obtained from the simulation were further compared with field measurements and are summarized in Table 2. The maximum breach depth, top width, and bottom width predicted by the model were 64 m, 285 m, and 130 m, respectively. These values differed from the measured data by 3 m, 15 m, and 40 m, respectively, indicating good agreement between the numerical results and observed field data.

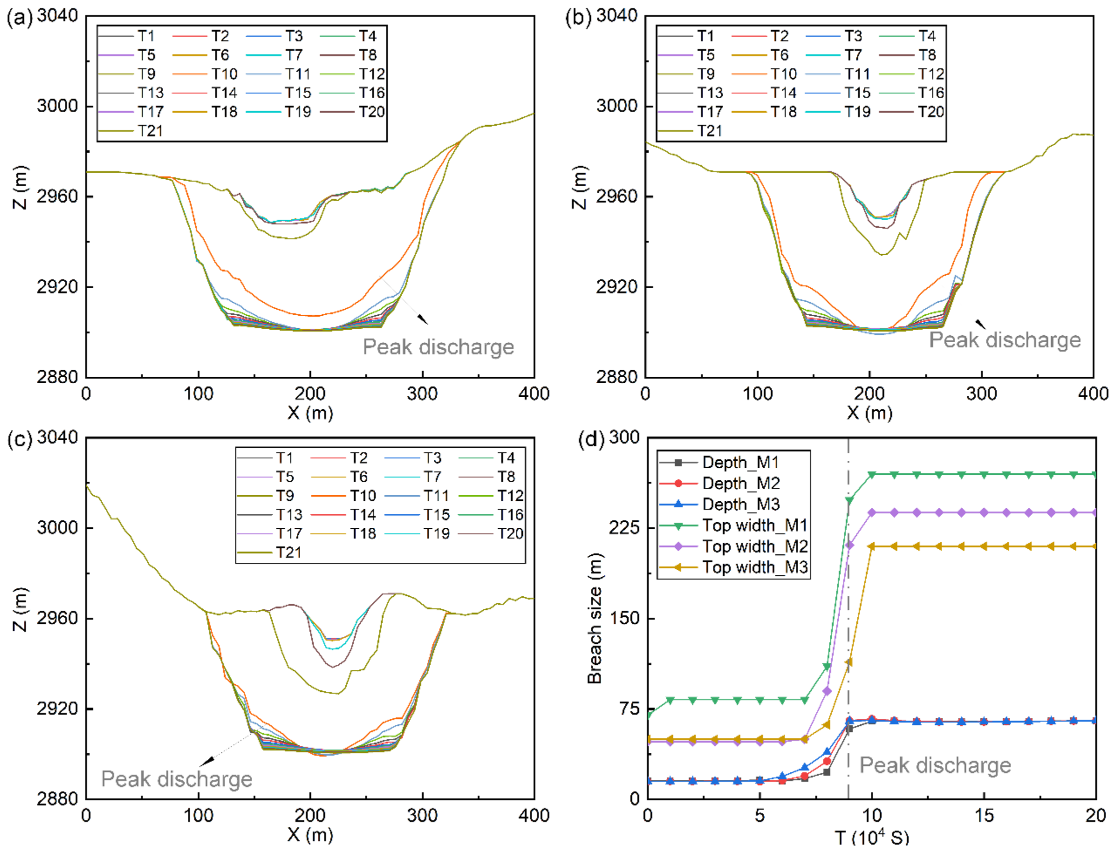

Figure 8 Variation of breach size during dam failure: (a) Breach at M1; (b) Breach at M2; (c) Breach at M3 and (d) Variation of breach depth and top width during dam failure. Note: T1 refers to the initiation of the overtopping failure, and the time interval between each line is 10,000 s.

Figure 9 presents the evolution of the dam geometry along the centerline of the diversion channel throughout the failure process. During the initial phase (from t = 0 to t = 70,000 s; profiles T1 to T7), no significant changes in dam geometry were observed, which corresponds to the relatively low discharge during this period. Between t = 70,000 s and t = 100,000 s, as discharge increased and reached its peak, the slope of the erosion surface steepened progressively, and substantial sediment removal occurred. The maximum slope of the erosion surface was observed at the time of peak discharge, indicating the most intense phase of erosion. Following the peak, the erosion surface slope gradually decreased until the dam reached its final topographic profile. Notably, the majority of erosion, breach development, and discharge variation occurred within the 70,000 s to 110,000 s window, highlighting this period as the most dynamic stage of the failure process. Interestingly, the evolution of the surface slope, characterized by an initial increase followed by a gradual decrease, was also observed in small-scale dam failure experiments (Coleman et al. 2002; Yang et al. 2024a), demonstrating consistency between numerical simulation and experimental findings.

Table 2 Comparison between the numerical results and field measurements

Parameters	Q_p (m^3/s)	T_p (h)	T_d (h)	$Z_{w,max}$ (m)	H_b (m)	W_t (m)	W_b (m)
Numerical results	32,767.0	27.8	54.0	2,955.73	64	285	130
Measured data	33,900.0	30	51.2	2,956.40	61	300	90
Errors	3.4%	7.3%	5.5%	0.02%	4.9%	5.0%	44.4%

Note: Q_p is the peak discharge, T_p is the time to peak discharge, T_d is the breach duration, $Z_{w,max}$ is the maximum water depth in the upstream reservoir, H_b is the breach depth, W_t and W_b are the breach top width and bottom width, respectively.

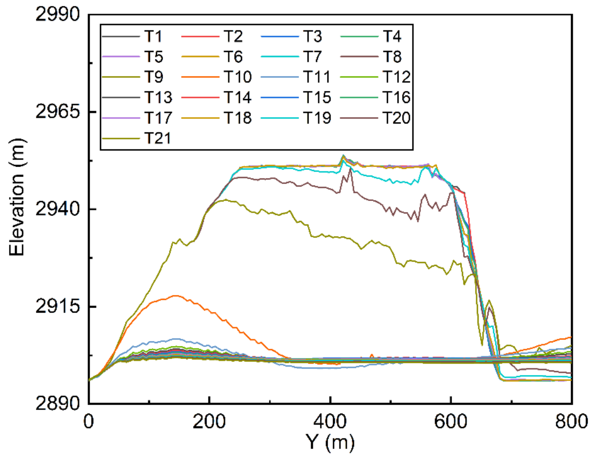

Figure 9 Dam geometry evolution along the centerline of the diversion channel. Note: T1 refers to the initiation of the overtopping failure, and the time interval between each line is 10,000 s.

4.1.3. Surface grain size distribution

Dam material composition controls the discharge variation during the dam failure. Additionally, erosion caused by water flow alters the surface grain size distribution, which in turn affects the evolution of dam topography. In the current simulation, an active layer depth of 0.7 m was adopted to capture sediment dynamics. While this depth may be relatively large for analyzing surface grain size variations, it appears as appropriate in this case due to the large discharges involved. Under such flow conditions, the model provides meaningful insights into the increase or decrease in surface sediment median diameter. Figure 10 shows the distribution of fine content (diameter smaller than 1.5 mm above 2,940 m and 3.3 mm below 2,940 m) and median diameter on the dam surface after the dam failure. As shown in Figure 10a, no significant change in surface fine content was observed following the dam failure. In terms of surface grain size distribution (Figure 10b), notable changes occurred only when the erosion front reached the lower sediment layer. A slight increase in median grain size was detected along the flow direction, but the overall variation remained relatively limited.

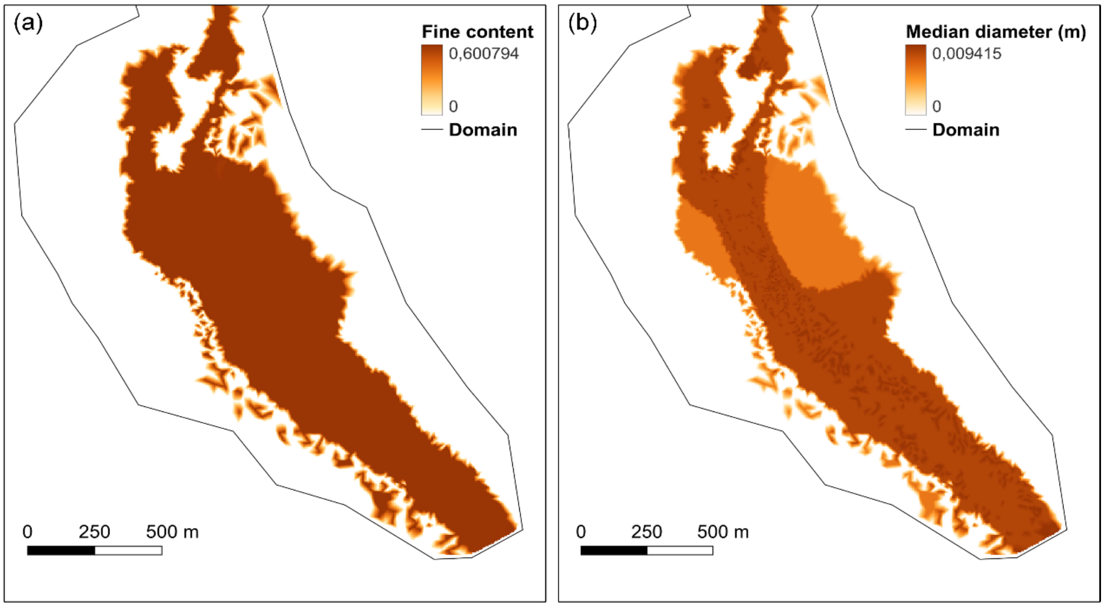

Figure 10 Variation of the surface grain size distribution after the failure of the second Baige landslide dam: (a) The content of sediments with median diameters of 1.5 and 3.3 mm and (b) Surface grain size distribution.

This observation can be attributed to the high discharge levels during the dam failure process, which created flow conditions well above the threshold for the incipient motion of the relatively fine sediments present in the dam material considered in the simulation. Under such high-energy conditions, all surface sediments were mobilized, limiting the formation of significant grain size sorting on the dam surface. According to Egiazaroff, (1965), the incipient motion of sediments with specific median diameters can be estimated as follow:

$$f = \theta_i - \theta_{ci} \tag{7}$$

where θ_i and θ_{ci} are the Shields number and the dimensionless critical shear stress of the sediment fractions with specific median diameters respectively, and can be calculated as follows:

$$\theta_i = \frac{n^2 u^2}{(s-1) d_{50,i} h^{1/3}} \tag{8}$$

$$\theta_{ci} = \begin{cases} \theta_c [\dfrac{log19}{\log\left(\dfrac{19 d_{50,i}}{d_{50}}\right)}]^2 & \dfrac{d_{50,i}}{d_{50}} \geq 0.4 \\ \theta_c \dfrac{d_{50}}{d_{50,i}} & \dfrac{d_{50,i}}{d_{50}} < 0.4 \end{cases} \tag{9}$$

where n is the Manning coefficient, u and h are the flow velocity and flow depth, respectively,

$s = 2.7$ is the ratio of grain density to water density, θ_c is the dimensionless critical shear stress of the whole sediment mixture and is considered as 0.047 during the simulation, $d_{50,i}$ and d_{50} are the median diameters of each sediment fraction and of the whole sediment mixture, respectively.

Figure 11 illustrates the variation of key parameters from Eqs. (7), (8), and (9) at three points along the diversion channel following the onset of overtopping failure. Both water depth and flow velocity initially increased and then decreased during the dam failure (Figure 11a), which in turn caused fluctuations in the Shields number for each sediment fraction. Notably, the Shields stress for finer sediments was significantly higher than for coarser sediments, with values being larger in the downstream section of the channel compared to the upstream section (Figure 11b). Furthermore, it is observed that the Shields number for sediments in each fraction remained significantly above the dimensionless critical shear stress (more than 1000 times larger in most cases), except at the onset of the overtopping failure. Under these conditions, all sediment fractions were eroded simultaneously, leading to no significant variation in the grain size distribution on the dam surface after the failure.

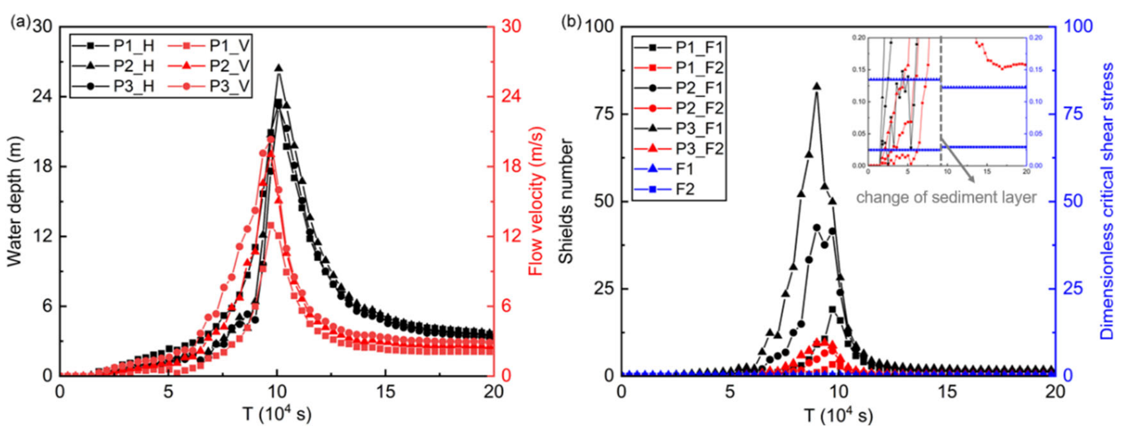

Figure 11 Variation of flow and erosion parameters at the points along the diversion channel (P1, P2 and P3 are located at M1, M2 and M3, respectively): (1) Variation of the water depth and flow velocity during dam failure; (b) Variation of the actual Shields number and the dimensionless critical shear stress during dam failure, with a zoom on low shear stress values. Note: F1 and F2 refer to the finer and coarser sediment fractions respectively, as shown in Table 1.

4.2. Influence of upstream inflow rate

Figure 12 presents the variation of both the peak discharge during dam failure and the time to peak discharge for the five scenarios, each considering different upstream inflow rates. It is important to note that the time to peak discharge also accounts for the time required to impound the upstream reservoir, adjusted for each scenario to account for the speed-up in reservoir filling during the computations. Therefore, the time to peak discharge in Figure 12 is calculated as follows:

$$T_P = 5000 \times \frac{80000}{Q_{in}} + T_{PS} - 80000 \tag{10}$$

where 5,000 m^3/s is the inflow rate used for the first 80,000 s of the numerical simulation to reduce the simulation time, T_{PS} is the time to peak discharge that was obtained from the numerical results.

The peak discharge increased from 29,600.7 m3/s to 37,232.8 m3/s as the upstream inflow discharge was raised from 400 m^3/s to 2,000 m^3/s (Figure 12a and b). Regarding the time to peak discharge, it took 265,795 s (73.8 h) from the formation of the dam to reach the peak discharge when the upstream inflow rate was 400 m^3/s. However, this duration decreased to 140,400 s (39.0 h) when the upstream inflow rate was increased to 2,000 m^3/s. In terms of the final breach size after the dam failure, both the breach depth and width increased with higher peak upstream discharge (Figure 13b). However, the variation in breach size was relatively small and can be considered negligible. For instance, when the inflow rate was increased from 400 m^3/s to 2,000 m^3/s, the final breach depth only increased by 4.9 m, which is 7.6% larger than that of S1 with the inflow rate of 400 m^3/s.

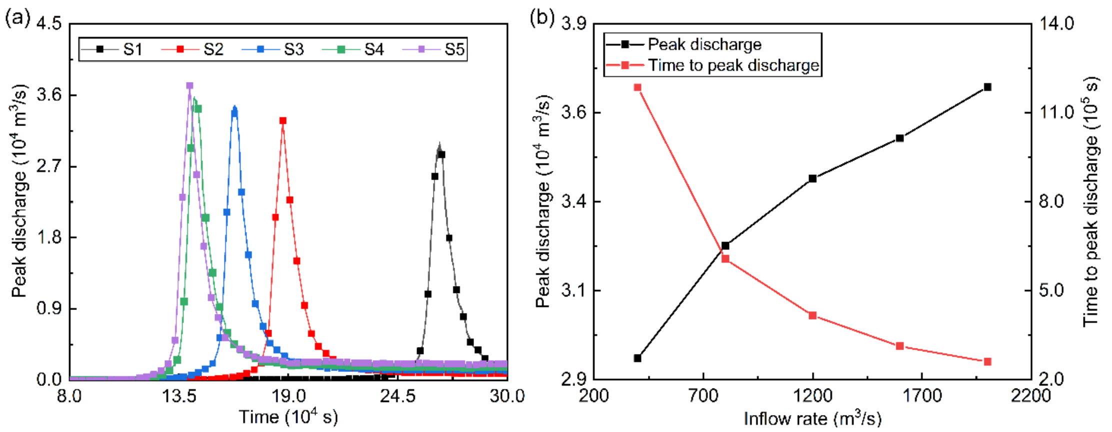

Figure 12 Influence of upstream inflow rate on the variation of diacharge during dam failure: (a) Discharge variation of S1 – S5 during dam failure; (b) Variation of the peak discharge and the time to peak discharge.

Previous flood routing analysis related to the failure of the second Baige landslide showed that there was no significant change in the downstream inundated area when the peak discharge increased from 33,900 m³/s to 55,579 m³/s (Yang et al., 2022). Therefore, while the upstream inflow rate influences the peak discharge resulting from the dam failure, its impact on downstream flood inundation is minimal. However, the significant reduction in the time to peak discharge is crucial, as it allows more time for local evacuation and the implementation of emergency countermeasures, such as the excavation of diversion channels at the dam crest. These actions help mitigate fatalities and economic losses in the affected areas.

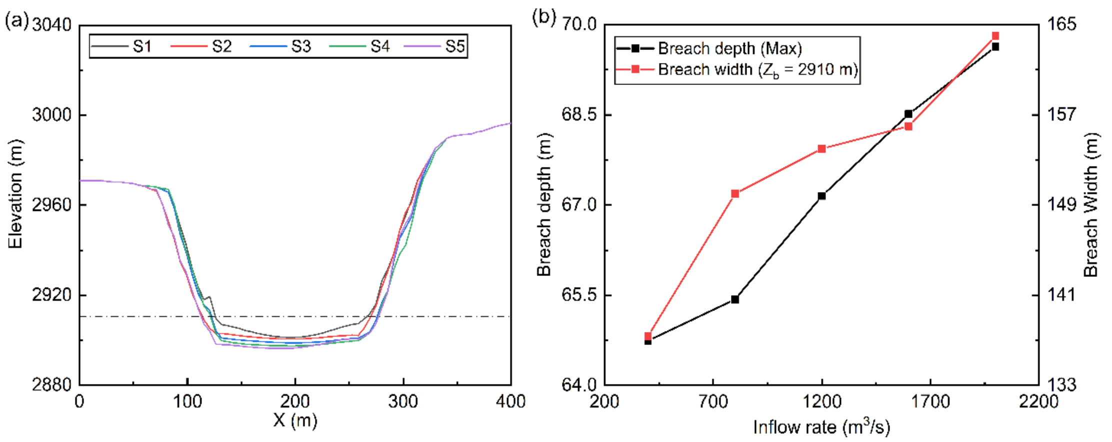

Figure 13 Influence of upstream inflow rate on breach evolution: (a) Final breach size of S1 – S5; (b) Variation of breach depth and breach width along the elevation of 2910 m.

4.3. Influence of dam material composition

Figure 14 illustrates the calculated discharge variation during the dam failure and the final breach size for two different sediment scenarios: non-uniform and multi-layered sediments (S2) and uniform and single-layered sediments (S6). Both scenarios yielded peak discharge and time to peak discharge values that were in good agreement with the field-measured data. The differences between the two scenarios were relatively small and can be considered negligible. For instance, in S6, a peak discharge of 34,770.6 m^3/s occurred 99,100 s after the initiation of overtopping failure, while in S2, the peak discharge was recorded at 32,767.0 m^3/s at 100,000 s after the failure began (Figure 14a). The difference in peak discharge and time to peak discharge between the two scenarios was 5.9% and 0.5%, respectively. As for the final breach size, a similar breach geometry was observed in both scenarios, with only minor differences. Along the three profiles (M1, M2, and M3), the final breach depth in S6, which considers uniform sediments, was consistently 1.6–1.7 m greater than that in S2. For example, the final breach depth along M1 was 2,900.6 m in S2 and 2,898.9 m in S6, showing a 1.7 m difference.

Additionally, the dam failure process in both scenarios was analyzed by comparing the variation in bed elevation and erosion rate during the failure at two points along profiles M1 and M2, as shown in Figure 15. After the initiation of the second Baige landslide dam failure, the bed elevation first decreased gradually and then experienced significant changes until the final breach size was reached. The erosion rate followed a similar pattern: it initially increased to its peak value corresponding to the peak discharge, then decreased until the final breach was observed. As with the discharge and breach size, the variations in bed elevation and erosion rate were quite similar between S2 and S6. The consistency in the results between the two scenarios can be explained by the incipient movement of sediment particles, as shown in Figure 11. The high inflow rate and the relatively fine sediments present in the second Baige landslide dam resulted in a complete erosion of all sediment particles across different diameters, leading to comparable erosion rates in both the non-uniform and uniform sediment scenarios.

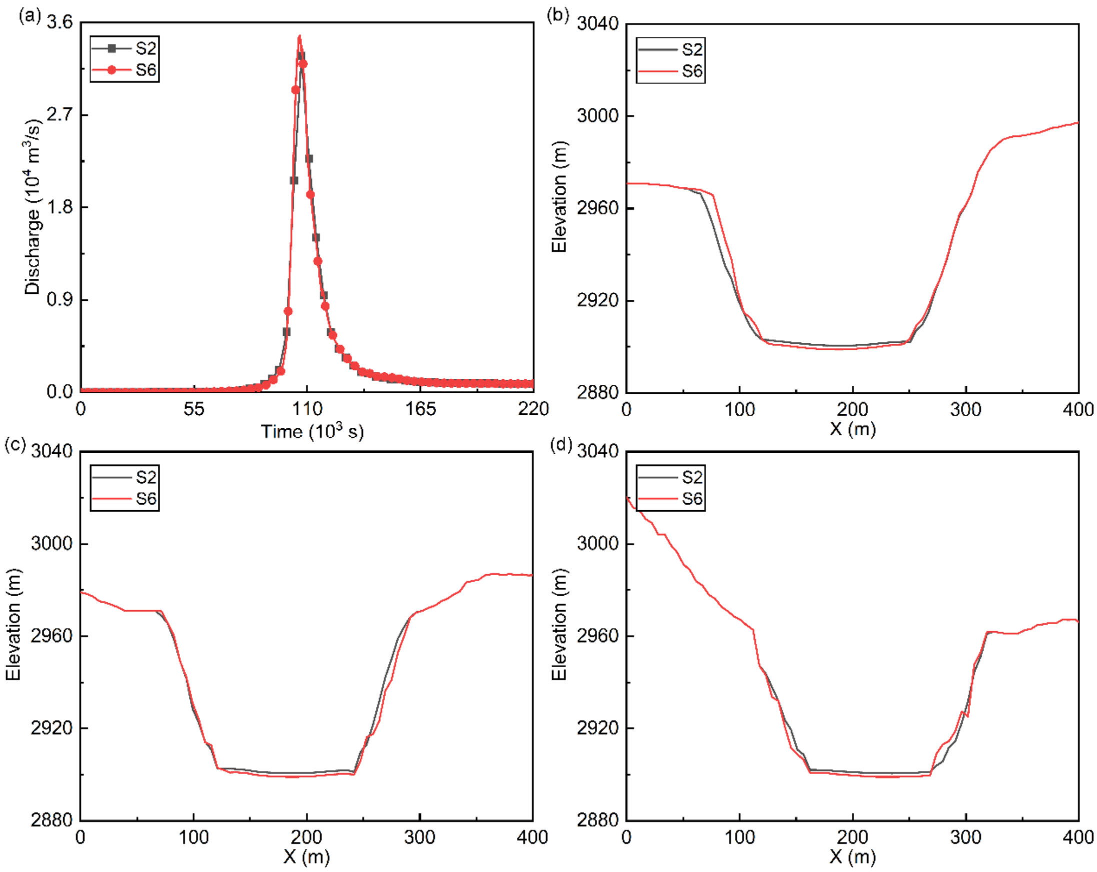

Figure 14 The variation of discharge during dam failure and final breach size considering different dam material compositions: (a) Discharge variation during dam failure; (b) The final breach size along M1, (c) along M2 and (d) along M3.

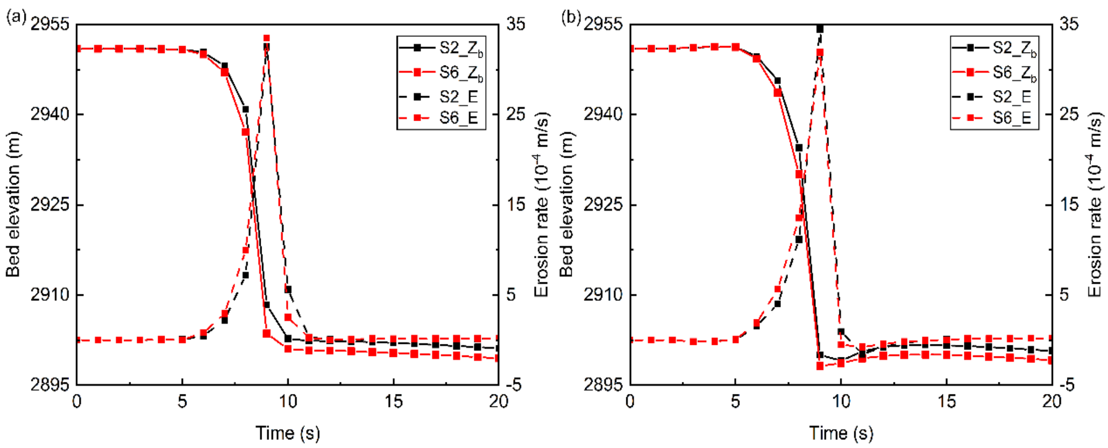

Figure 15 Comparison of bed elevation and erosion rate variation during dam failure between S2 and S6: (a) P1 on M1; (b) P2 on M2. Note: Z_b is the bed elevation; E is erosion rate and is calculated as $E = \Delta Z_b / \Delta t$.

5. Discussion

5.1. Comparison of numerical results obtained from different models

In this section, a model based on an empirical equation and a simplified physically based model are applied to calculate the dam failure parameters for the second Baige landslide dam. Additionally, two other detailed models (Mei et al. 2022; Li et al. 2023) are used to further validate the accuracy and effectiveness of the proposed approach.

Table 3 provides a brief introduction and the main characteristics of the selected models, including the proposed approach referred to as Yand et al. (2024). For the empirical equation, the model proposed by Peng and Zhang, (2012) was selected. This model was developed based on regression analysis of landslide dam parameters from several case studies, using data from 45, 21, 13, and 10 landslide dam cases to derive equations predicting peak discharge, breach depth, and breach top and bottom widths, respectively. The model also incorporates material characteristics of the dam through an empirical parameter representing the dam's erodibility. For the simplified physically-based numerical model, the DABA model proposed by Chang and Zhang, (2019) was considered. This model applies the broad-crested weir flow equation to calculate the discharge during dam failure and assumes a breach evolution pattern with an erosion rate calculated by Eq. (16) to simulate the breach development. Regarding the detailed numerical models, results from a 2D double layer-averaged two-phase flow model proposed by Li et al. (2023) and a 3D model based on Reynolds-averaged Navier–Stokes (RANS) equations proposed by Mei et al. (2022) were also compared.

Table 3 Introduction and characteristics of models used for predicting dam failure parameters.

Reference	Category	Conception	Remark

Peng and Zhang, (2012)	Empirical equation	1) Regression analysis: $\frac{Q_p}{\left(\frac{g^{1/2}}{H_d^{5/2}}\right)} = (\frac{H_d}{H_r})^{-1.371} \left(\frac{V_l^{1/3}}{H_d}\right)^{1.536} e^{\alpha}$ (11) $\frac{H_b}{H_r} = (\frac{H_d}{H_r})^{0.923} \left(\frac{V_l^{1/3}}{H_d}\right)^{0.118} e^{\alpha}$ (12) $\frac{W_t}{H_r} = (\frac{H_d}{H_r})^{0.911} \left(\frac{V_l^{1/3}}{H_d}\right)^{0.271} e^{\alpha}$ (13) $\frac{W_b}{H_d} = 0.003 \left(\frac{H_d}{H_r}\right) + 0.07 \left(\frac{V_l^{1/3}}{H_d}\right) + \alpha$ (14)	1) Limited case number (45, 21, 13, 10 landslide dam cases for Q_p, H_b, W_t and W_b; 2) Erodibility of the material should be evaluated to determin α.
Chang and Zhang, (2010)	Simplified physically-based model	1) The broad-crested weir flow equation: $Q_p = 1.7[W_b + (H - Z)tan\theta](H - Z)^{\frac{3}{2}}$ (15) 2) Erosion rate calculation: $E = k_d(\tau - \tau_c)$ (16) 3) Breach development: 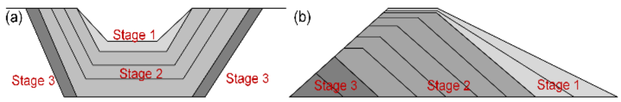 Across the channel along the channel	1) The breach development pattern across and along the flow directions should be assumed.
Mei et al, (2022)	3D RANS equations-based model	1) RANS equations for flow field. 2) RNG k-ε turbulence model for nonlinear Reynolds stress term. 3) Update bed elevation: The Exner equation. 4) Uniform sediments with both bed and suspend loads.	1) Grain size distribution of the dam material. 2) Turbulent coefficients.
Li et al, (2023)	2D double layer-averaged two-phase flow model	1) Equations for Upper clear-water flow layer. 2) Equations for lower water-sediment mixture flow layer. 3) Equations for size-specific sediment phase. 4) Update bed elevation: The Exner equation.	1) Grain size distribution of the dam material. 2) Boundary of the two flow layers.
Yang et al, (2024)	2D model considering non-uniform and multi-layered sediments	1) Update flow parameters: Shallow water equations Eq. (1) (2) and (3). 2) Update bed elevation: The modified Exner equation Eq. (4). 3) Update surface grain size distribution: Hirano's active layer equation Eq. (5). 4) Multi-layered sediments	1) Grain size distribution of the dam material. 2) Sediment layers´ depth.

Note: Q_p is the peak discharge, g is the gravitational acceleration, H_d and H_r are the dam height and reference height (1 m), respectively; V_l is the upstream lake volume, W_t and W_b are the breach top and bottom width, respectively; α is the erodibility factor and varies in each equation. H and Z are the water level and sediment level, respectively; θ is the side slope of the breach. E is the erosion rate, k_d is the coefficient of erodibility, τ and τ_c are the shear stress at the water/soil interface and critical shear stress of the soil.

Table 4 presents the dam failure parameters of the second Baige landslide dam obtained from the five models. When compared to the simplified and the proposed detailed physically-based numerical models, the empirical equations underestimated the peak discharge but overestimated the final breach size, particularly the breach depth and breach top width, with differences of 30.82% and 49.90%, respectively. The best estimate for the peak discharge of 34,348.0 m^3/s (compared to the measured value of 33,900.0 m^3/s, yielding a difference of just 1.32%) was obtained from the simplified physically-based DABA model. However, the DABA model overestimated the final breach size, especially the breach bottom width, which was estimated at 139.8 m, a difference of more than 50% compared to the measured data of 90 m. Regarding the detailed physically-based numerical model used in this study, good agreement was found with the field data for peak discharge, breach depth, and breach top width. Specifically, the smallest errors of 4.92% and 5.00% were obtained for the final breach depth and breach top width, respectively. However, similar to the DABA model, the detailed model overestimated the final breach bottom width, with a difference of 44.44% compared to the field data. This discrepancy can be attributed to the neglected variation of the angle parameters in the bank failure module: these parameters can indeed change due to sediment layer changes during the simulation, but here a constant value was applied, leading to possible inaccurate estimate of the breach width. Furthermore, an unsaturated state in the dam material was observed, but it could not be simulated with the current model. Therefore, further development of the numerical model is needed in future studies. Nevertheless, it has the advantage of not being limited by the case numbers used to validate formulas or the assumed breach pattern, unlike the other models.

Regarding the other two detailed numerical models, only the peak discharge during dam failure is available. As shown in Table 4, the 3D RANS-based model proposed by Mei et al. (2022) underestimates the peak discharge, with an error of 12.92% (29,518.0 m^3/s vs. 33,900.0 m^3/s). A smaller error of 3.28% (32,787.0 m³/s vs. 33,900.0 m³/s) is observed with the 2D double-layered two-phase flow model proposed by Li et al. (2023). This result is in good agreement with the one obtained by the proposed model, which considers non-uniform and multi-layered sediments, showing a difference of only 20 m³/s. Therefore, despite the larger error in predicting the breach bottom width, the proposed numerical model remains well suited to simulate the dam failure process and predicting the relevant failure parameters.

Table 4 Comparison of dam failure parameters obtained from different models

Model	Parameter	Q_p	H_b	W_t	W_b
Empirical equation*	Estimated	30,515.0	42.2	150.3	114.2
	Errors	9.99%	30.82%	49.90%	26.89%
Simplified model*	Estimated	34,348.0	70.5	337.4	139.8
	Errors	1.32%	15.57%	12.47%	55.33%
Detailed model (Mei et al, 2022)	Estimated	29,518.0	-	-	-
	Errors	12.92%	-	-	-
Detailed model (Li et al, 2023)	Estimated	32,787.0	-	-	-
	Errors	3.28%	-	-	-
Detailed model (Yang et al, 2024b)	Estimated	32,767.0	64.0	285.0	130.0
	Errors	3.34%	4.92%	5.00%	44.44%

Note: *The results was cited from Zhang et al, (2019). Q_p (m^3/s) is the peak discharge; H_b (m) is the breach depth; W_t (m) is the breach top width and W_b (m) is the breach bottom width.

5.2. Does material composition really influence the dam failure process?

The above results indicate that the dam material composition, whether uniform sediments or non-uniform and multi-layered sediments, has a limited effect on the failure process and discharge variation in the case of the second Baige landslide dam. This can be attributed to the high inflow rate combined with the fine material composition, which leads to the erosion of all sediments within the dam, regardless of their median diameters. However, it is important to note that the inflow conditions and material compositions of landslide dams can vary significantly depending on local environmental and geological factors. For instance, the Tangjiashan landslide, triggered by the 2008 Wenchuan earthquake in Sichuan Province, China, consisted of multiple sediment layers, with a non-erodible rock layer at the bottom of the dam. In contrast, the Tsaoling landslide dam, caused by the 1999 Chichi earthquake in Taiwan, experienced a much lower inflow rate of 17.9 m^3/s. In these cases, overtopping flow may erode only some fractions of the bed material, potentially leading to significant differences between results derived from uniform, single-layered sediments and non-uniform, multi-layered sediments. Consequently, further case studies are necessary to evaluate the performance of the model when considering non-uniform and multi-layered sediments.

5.3. Limitations on modelling landslide dam failure

Although the proposed numerical model successfully simulates the dam failure process and predicts the associated failure parameters, there are three key limitations that should be addressed in future work. First, the bank failure module should account for the variation of bank material properties and water content during the failure process to better simulate the variation in breach size during dam failure by . Second, the numerical modeling in this study primarily focused on the dam failure with mesh sizes ranging from 5 m to 100 m and a limited size of the simulated area, and the total simulation time was estimated to be 5 hours. However, landslide dam failure can have significant downstream impacts, including both flooding and morphological changes. Therefore, it is crucial to extend the simulation to account for these downstream effects. This requires a larger computational domain that includes the entire potentially impacted downstream area. Therefore, the computational efficiency of the model must be improved to allow for such large-scale simulations within a reasonable time frame. Third, most landslide dams consist of materials with particle sizes ranging from millimeters to several meters. Current numerical tools are not well-equipped to simulate landslide dam failure involving large particles, as the commonly used sediment transport equations were not designed to account for rock movements. Addressing the influence of large particles remains a major challenge for the existing numerical techniques.

6. Conclusion

This study applied a 2D numerical model incorporating non-uniform and multi-layered sediments to simulate the failure of the second Baige landslide dam considering various upstream inflow rates into the artificially formed reservoir and dam material compositions. The 2D model demonstrated good accuracy in simulating the dam failure process and the corresponding parameter variations. The estimated peak discharge was 32,767.0 m^3/s, with a 3.61% difference compared to the measured value. The estimated final breach depth, breach top width, and breach bottom width were 64 m, 285 m, and 130 m, respectively, with errors of 4.9%, 5.0%, and 44.4% compared to field data. Changing the inflow rate in the artificial upstream reservoir has a significant effect on the peak discharge, while the effect on the final breach depth and width was small enough to be considered negligible. Notably, a reduced inflow rate that extends the time required to fill the upstream reservoir significantly delayed the dam failure, providing more time for emergency mitigation measures. In the present case, the material composition showed a limited impact on the failure process: scenarios with uniform single-layered and non-uniform multi-layered sediments resulted in similar discharge variations and breach sizes, with only a 5.9% difference in peak discharge and a 1.7 m difference in final breach depth. Furthermore, when non-uniform multi-layered sediment was considered, no significant variation in the surface grain size distribution was observed after the dam failure. This similarity and the unchanged surface grainsize distribution are attributed to the high inflow discharge, which generated bed shear stresses far above the threshold for incipient sediment movement, resulting in similar erosion rates regardless of the material composition.

Moreover, the numerical results from the proposed model were compared with those from empirical equations and a simplified physically-based model. All models accurately simulated peak discharge, with errors within 10%. However, empirical equations tended to overestimate the breach size due to the limited real case data used in the regression analysis. While the simplified physically-based model and the proposed model performed better in simulating breach size, the simplified model's assumptions regarding failure patterns limit its applicability in varied conditions. Compared to two other detailed models, the proposed detailed model offered a more accurate representation of the failure process, breach evolution, and discharge variation.

Finally, this study enhances the understanding of landslide dam failure and supports hazard management in mountainous regions, highlighting the key role of controlling the upstream inflow discharge when possible. Further model refinement and validation using real-case scenarios are planned to improve its reliability and performance, especially regarding the effect of multiple grain sizes in the dam material that is known from experimental studies to significantly affect the failure process.

References

ASCE/EWRI Task Committee on Dam/Levee Breaching. (2011). Earthen embankment breaching. Journal of hydraulic engineering, 137(12), 1549-1564. https://doi.org/10.1061/(ASCE)HY.1943-7900.0000498

Chang, D. S., & Zhang, L. M. (2010). Simulation of the erosion process of landslide dams due to overtopping considering variations in soil erodibility along depth. Natural Hazards and Earth System Sciences, 10(4), 933-946. https://doi.org/10.5194/nhess-10-933-2010

Chavarrías, V., Arkesteijn, L., & Blom, A. (2019). A well-posed alternative to the Hirano active layer model for rivers with mixed-size sediment. Journal of Geophysical Research: Earth Surface, 124(11), 2491-2520. https://doi.org/10.1029/2019JF005081

Costa, J. E., & Schuster, R. L. (1988). The formation and failure of natural dams. Geological society of America bulletin, 100(7), 1054-1068. https://doi.org/10.1130/0016-7606(1988)

Delaney, K. B., & Evans, S. G. (2015). The 2000 Yigong landslide (Tibetan Plateau), rockslide-dammed lake and outburst flood: Review, remote sensing analysis, and process modelling. Geomorphology, 246, 377-393. https://doi.org/10.1016/j.geomorph.2015.06.020

Delpierre, N., Rattez, H., & Soares-Frazao, S. (2023). Finite-volume coupled surface-subsurface flow modelling in earth dikes. Journal of Hydraulic Research, 61(5), 754-763. https://doi.org/10.1080/00221686.2023.2246936

Egiazaroff, I. V. (1965). Calculation of nonuniform sediment concentrations. Journal of the Hydraulics Division, 91(4), 225-247. https://doi.org/10.1061/JYCEAJ.0001277

Evangelista, S., Greco, M., Iervolino, M., Leopardi, A., & Vacca, A. (2015). A new algorithm for bank-failure mechanisms in 2D morphodynamic models with unstructured grids. International Journal of Sediment Research, 30(4), 382-391. https://doi.org/10.1016/j.ijsrc.2014.11.003

Franzini, F., & Soares-Frazão, S. (2016). Efficiency and accuracy of Lateralized HLL, HLLS and Augmented Roe's scheme with energy balance for river flows in irregular channels. Applied mathematical modelling, 40(17-18), 7427-7446. https://doi.org/10.1016/j.apm.2016.02.007

Froehlich, D. C. (2022). Peak flood discharge from a landslide dam outburst. Natural Hazards Review, 23(2), 04022001. https://doi.org/10.1061/(ASCE)NH.1527-6996.0000545

García-Navarro, P., Murillo, J., Fernández-Pato, J., Echeverribar, I., & Morales-Hernández, M. (2019). The shallow water equations and their application to realistic cases. Environmental Fluid Mechanics, 19, 1235-1252. https://doi.org/10.1007/s10652-018-09657-7

Hashemi, S., Carrivick, J., & Klaar, M. (2024). Hydromorphological response of heavily modified rivers to flood releases from reservoirs: A case study of the Spöl River, Switzerland. Earth Surface Processes and Landforms, 49(3), 1028-1046. https://doi.org/10.1002/esp.5749

Juez, C., Ferrer-Boix, C., Murillo, J., Hassan, M. A., & García-Navarro, P. (2016). A model based on Hirano-Exner equations for two-dimensional transient flows over heterogeneous erodible beds. Advances in Water Resources, 87, 1-18. https://doi.org/10.1016/j.advwatres.2015.10.013

Korup, O. (2004). Geomorphometric characteristics of New Zealand landslide dams. Engineering Geology, 73(1-2), 13-35. https://doi.org/10.1016/j.enggeo.2003.11.003

Li, J., Cao, Z., Cui, Y., Fan, X., Yang, W., Huang, W., & Borthwick, A. (2021). Hydro-sediment-morphodynamic processes of the baige landslide-induced barrier Lake, Jinsha River, China. Journal of Hydrology, 596, 126134. https://doi.org/10.1016/j.jhydrol.2021.126134

Li, Y., Fan, X., & Cheng, G. (2006). Landslide and rockfall distribution by reservoir of stepped hydropower station in the Jinsha River. Wuhan Univ. J. Natural Sci. 11 (4), 801–805. https://doi.org/10.1007/BF02830167

Li, Z., Özgen-Xian, I., & Maina, F. Z. (2021). A mass-conservative predictor-corrector solution to the 1D Richards equation with adaptive time control. Journal of Hydrology, 592, 125809. https://doi.org/10.1016/j.jhydrol.2020.125809

Martínez-Aranda, S., Murillo, J., & García-Navarro, P. (2022). A GPU-accelerated Efficient Simulation Tool (EST) for 2D variable-density mud/debris flows over non-uniform erodible beds. Engineering Geology, 296, 106462. https://doi.org/10.1016/j.enggeo.2021.106462

Mei, S., Chen, S., Zhong, Q., & Shan, Y. (2022). Detailed numerical modeling for breach hydrograph and morphology evolution during landslide dam breaching. Landslides, 19(12), 2925-2949. https://doi.org/10.1007/s10346-022-01952-1

Meurice, R., & Soares-Frazão, S. (2024). Machine learning rather than trial and error to close morphodynamical tuneable parameters: Application to a two-phase/two-layer model. Journal of Hydroinformatics, 26(4), 744-761. https://doi.org/10.2166/hydro.2024.183

Ouyang, C., An, H., Zhou, S., Wang, Z., Su, P., Wang, D., Cheng D., & She, J. (2019). Insights from the failure and dynamic characteristics of two sequential landslides at Baige village along the Jinsha River, China. Landslides, 16, 1397-1414. https://doi.org/10.1007/s10346-019-01177-9

Peng, M., & Zhang, L. M. (2012). Breaching parameters of landslide dams. Landslides, 9, 13-31. https://doi.org/10.1007/s10346-011-0271-y

Pudasaini, S. P. (2012). A general two-phase debris flow model. Journal of Geophysical Research: Earth Surface, 117(F3). https://doi.org/10.1029/2011JF002186

Qian, H., Cao, Z., Liu, H., & Pender, G. (2017). Numerical modelling of alternate bar formation, development and sediment sorting in straight channels. Earth Surface Processes and Landforms, 42(4), 555-574. https://doi.org/10.1002/esp.3988

Sassa, K. (2005). Landslide disasters triggered by the 2004 Mid-Niigata Prefecture earthquake in Japan. Landslides, 2(2), 135-142. https://doi.org/10.1007/s10346-005-0054-4

Shen, D., Shi, Z., Peng, M., Zhang, L., & Jiang, M. (2020). Longevity analysis of landslide dams. Landslides, 17, 1797-1821. https://doi.org/10.1007/s10346-020-01386-7

Shen, D., Shi, Z., Zheng, H., Yang, J., & Hanley, K. J. (2022). Effects of grain composition on the stability, breach process, and breach parameters of landslide dams. Geomorphology, 413, 108362. https://doi.org/10.1016/j.geomorph.2022.108362

Shi, Z. M., Xiong, X., Peng, M., Zhang, L. M., Xiong, Y. F., Chen, H. X., & Zhu, Y. (2017). Risk assessment and mitigation for the Hongshiyan landslide dam triggered by the 2014 Ludian earthquake in Yunnan, China. Landslides, 14, 269-285. https://doi.org/10.1007/s10346-016-0699-1

Simpson, G., & Castelltort, S. (2006). Coupled model of surface water flow, sediment transport and morphological evolution. Computers & Geosciences, 32(10), 1600-1614. https://doi.org/10.1016/j.cageo.2006.02.020

Soares-Frazão, S., & Zech, Y. (2011). HLLC scheme with novel wave-speed estimators appropriate for two-dimensional shallow-water flow on erodible bed. International journal for numerical methods in fluids, 66(8), 1019-1036. https://doi.org/10.1002/fld.2300

Soares-Frazao, S., Canelas, R., Cao, Z., Cea, L., Chaudhry, H. M., Die Moran, A., ... & Zech, Y. (2012). Dam-break flows over mobile beds: experiments and benchmark tests for numerical models. Journal of Hydraulic Research, 50(4), 364-375. https://doi.org/10.1080/00221686.2012.689682

Stecca, G., Siviglia, A., & Blom, A. (2014). Mathematical analysis of the S aint-V enant-H irano model for mixed-sediment morphodynamics. Water Resources Research, 50(10), 7563-7589. https://doi.org/10.1002/2014WR015251

Swartenbroekx, C., Soares-Frazão, S., Staquet, R., & Zech, Y. (2010). Two-dimensional operator for bank failures induced by water-level rise in dam-break flows. Journal of Hydraulic Research, 48(3), 302-314. https://doi.org/10.1080/00221686.2010.481856

Takayama, S., Miyata, S., Fujimoto, M., & Satofuka, Y. (2021). Numerical simulation method for predicting a flood hydrograph due to progressive failure of a landslide dam. Landslides, 18(11), 3655-3670. https://doi.org/10.1007/s10346-021-01712-7

Tan, Y., Liu, H., & Lu, Y. (2024). Predicting soil erosion and sediment delivery in large, data-sparse, mountainous basins. Earth Surface Processes and Landforms, 49(6), 1778-1795. https://doi.org/10.1002/esp.5797

Thapa, S., Sinclair, H. D., Creed, M. J., Mudd, S. M., Attal, M., Borthwick, A. G., Ghimire, B. N., & Watson, C. S. (2024). The impact of sediment flux and calibre on flood risk in the Kathmandu Valley, Nepal. Earth Surface Processes and Landforms, 49(2), 706-727. https://doi.org/10.1002/esp.5731

Van Tien, P., Luong, L. H., Sassa, K., Takara, K., Sumit, M., Thanh Nhan, T., Dang, K., & Minh Duc, D. (2021). Mechanisms and modeling of the catastrophic landslide dam at Jure Village, Nepal. Journal of Geotechnical and Geoenvironmental Engineering, 147(11), 05021010. https://doi.org/10.1061/(ASCE)GT.1943-5606.000263

Walder, J. S., & O'Connor, J. E. (1997). Methods for predicting peak discharge of floods caused by failure of natural and constructed earthen dams. Water Resources Research, 33(10), 2337-2348. https://doi.org/10.1029/97WR01616

Wang, B., Yang, S., & Chen, C. (2022). Landslide dam breaching and outburst floods: A numerical model and its application. Journal of Hydrology, 609, 127733. https://doi.org/10.1016/j.jhydrol.2022.127733

Wu, W., & Wang, S. S. (2007). One-dimensional modeling of dam-break flow over movable beds. Journal of hydraulic engineering, 133(1), 48-58. https://doi.org/10.1061/(ASCE)0733-9429(2007)133:1(48)

Xia, C. C., Li, J., Cao, Z. X., Liu, Q. Q., & Hu, K. H. (2018). A quasi single-phase model for debris flows and its comparison with a two-phase model. Journal of Mountain Science, 15(5), 1071-1089. https://doi.org/10.1007/s11629-018-4886-5

Yang, J., Shi, Z., Peng, M., Zheng, H., Soares-Frazão, S., Zhou, J., Shen, D., & Zhang, L. (2022). Quantitative risk assessment of two successive landslide dams in 2018 in the Jinsha River, China.

Engineering Geology, 304, 106676. https://doi.org/10.1016/j.enggeo.2022.106676

Yang, J., Shi, Z., Soares-Frazão, S., Zheng, H., & Shen, D. (2024a). Influence of dam and erodible bed material composition on landslide dam failure and induced morphological changes: an experimental study. Bulletin of Engineering Geology and the Environment, 83(2), 61. https://doi.org/10.1007/s10064-024-03556-6

Yang, J., Soares-Frazao, S., Shi, Z., & Shen, D. (2024b). A 2D numerical model for simulating landslide dam failure and induced morphological changes considering multi-layer and non-uniform sediments. Journal of Hydroinformatics, jh2024103. https://doi.org/10.2166/hydro.2024.103

Yin, Y., Wang, F., & Sun, P. (2009). Landslide hazards triggered by the 2008 Wenchuan earthquake, Sichuan, China. Landslides, 6, 139-152. https://doi.org/10.1007/s10346-009-0148-5

Zhao, J., Özgen-Xian, I., Liang, D., Wang, T., & Hinkelmann, R. (2019). A depth-averaged non-cohesive sediment transport model with improved discretization of flux and source terms. Journal of hydrology, 570, 647-665. https://doi.org/10.1016/j.jhydrol.2018.12.059

Zhang, L., Xiao, T., He, J., & Chen, C. (2019). Erosion-based analysis of breaching of Baige landslide dams on the Jinsha River, China, in 2018. Landslides, 16, 1965-1979. https://doi.org/10.1007/s10346-019-01247-y

Zheng, H., Shi, Z., Shen, D., Peng, M., Hanley, K. J., Ma, C., & Zhang, L. (2021). Recent advances in stability and failure mechanisms of landslide dams. Frontiers in Earth Science, 9, 659935. https://doi.org/10.3389/feart.2021.659935